



High-resolution 4D ERT monitoring of recently deglaciated sediments undergoing freeze-thaw transitions in the High Arctic

5 Mihai O. Cimpoiasu¹, Oliver Kuras¹, Harry Harrison¹, Paul B. Wilkinson¹, Phillip Meldrum¹,
Jonathan E. Chambers¹, Dane Liljestr and², Carlos Oroza², Steven K. Schmidt³, Pacifica
Sommers³, Lara Vimercati³, Trevor P. Irons⁴, Zhou Lyu⁵, Adam Solon⁵, and James A.
Bradley^{5,6}

10 ¹ Environmental and Engineering Geophysics, British Geological Survey, United Kingdom

² University of Utah, Salt Lake City, Utah, United States of America

³ University of Colorado, Boulder, Colorado, United States of America

⁴ Montana Technical University, Butte, Montana, United States of America

⁵ School of Biological and Behavioural Sciences, Queen Mary University of London, London, UK

15 ⁶ Aix Marseille University, Universit  de Toulon, CNRS, IRD, MIO, Marseille, France

Correspondence to: Mihai O. Cimpoiasu (mcim@bgs.ac.uk)

20

25

30

35

40

45

50



Abstract. Arctic regions are under immense pressure from a continuously warming climate. Understanding the physical mechanisms and processes that determine soil liquid moisture availability contributes to the way we conceptualize and understand the development and functioning of terrestrial Arctic ecosystems. However, harsh weather and logistical constraints limit opportunities to directly observe subsurface processes year-round, hence automated and uninterrupted strategies of monitoring soil physicochemical properties are essential. Geoelectrical monitoring using electrical resistivity tomography (ERT) has proven to be an effective method to capture soil moisture distribution in time and space. ERT instrumentation has been adapted for year-round operation in high-latitude weather conditions. We installed two geoelectrical monitoring stations on the forefield of a retreating glacier on Svalbard, consisting of semi-permanent surface ERT arrays and co-located soil sensors, which track seasonal changes in 3D of soil electrical resistivity, moisture and temperature. One of the stations observes recently exposed sediments (5-10 years since deglaciation), whilst the other covers more established sediments (50 years since deglaciation). We obtained a one-year continuous measurement record (Oct 2021–Sep 2022), which produced 4D images of soil freeze-thaw transitions with unprecedented detail, allowing us to calculate the velocity of the thawing front in 3D. At its peak, this was found to be 1 m/day for the older sediments and 0.4 m/day for the younger sediments. Records of soil moisture and thermal regime obtained by sensors help define the conditions under which snowmelt takes place. Our data reveal that the freeze-thaw shoulder period, during which the surface soils experienced the zero-curtain effect, lasted 23 days at the site closer to the glacier, but only 6 days for the older sediments. Furthermore, we used unsupervised clustering to classify areas of the soil volume according to their electrical resistivity coefficient of variance, which enables us to understand spatial variations in susceptibility to water phase transition. Novel insights about soil moisture dynamics throughout the spring melt will help parameterize models of biological activity to build a more predictive understanding of newly emerging terrestrial landscapes and their impact on carbon and nutrient cycling.

1 Introduction

The Arctic has experienced increases in average air temperature and annual precipitation in recent decades (Rapaic et al., 2015; Rawlins et al., 2010). This has led to a reduction of the permanent ice volume, with the Svalbard Archipelago alone losing approximately 5,000 km² of terrestrial glacier cover since the beginning of the 20th century (Martin-Moreno et al., 2017).

The till-covered landscapes emerging from beneath the retreating ice are rapidly colonized by microorganisms during the initial stages of soil formation (Schmidt et al., 2008; Bradley et al., 2014) and are sensitive to further climatological changes (Bradley et al., 2017). Deeper layers of the soil undergo successional changes more slowly than surface layers (Rime et al., 2015) and are likely to be carbon-limited due to a lack of photosynthetically derived organic carbon (Freeman et al., 2009). Deeper layers may therefore be less sensitive to changes in key drivers of soil biological activity such as moisture and temperature.

An enormous carbon pool is estimated to be stored in Arctic soils with mean annual temperatures below freezing (< 0°C) (Hugelius et al., 2014). These soils are highly vulnerable to climate warming, which causes thawing of permafrost and accelerates carbon mobilization and decomposition processes, thus elevating rates of carbon exchange between soil and the atmosphere. Recent studies have observed continuous soil respiration fluxes from Arctic soils during winter periods (Arndt et al., 2020; Natali et al., 2019) as well as bursts of carbon emitted from soils following early spring thawing (Nielsen et al., 2001; Raz-Yaseef et al., 2017; Teepe & Ludwig, 2004). Records have also captured considerable CO₂ emissions from Arctic soils during both of the shoulder seasons – i.e., not only during the springtime thawing, but also during fall freezing (Commene et al., 2017; Zona et al., 2016). Soil moisture content availability and temperature are known to strongly influence soil biological activity and consequently respiration (Brooks et al., 1997; Elberling & Brandt, 2003; Schmidt et al., 2009). Quantifying moisture variability across pioneer soils along with occurrences of spring snowmelt would greatly improve our understanding of where, when, and for how long, microbial communities are active in these early successional landscapes, and thus can contribute to biologically driven carbon transformations. However, repeat surveying or sampling in the Arctic can be challenging due to harsh weather conditions (especially under snow cover during winter months) and distance from population centres; thus, a remote, autonomous method of monitoring such environments is desirable.

The emergence of year-round data (e.g., Boike et al., 2018) will undoubtedly enable an improved understanding and prediction of the fate of Arctic soils under future warming scenarios. Electrical resistivity tomography (ERT) is a ground investigation method that provides a fast, cost-effective and minimally invasive way of imaging and monitoring soil moisture (Michot et al., 2003; Cimpoiasu et al., 2020). ERT has an extensive track record of applications in the field (Loke et al., 2013), including polar environments where it was used for its sensitivity to ice content (Wu et al., 2013, 2017), a weak electrolyte (Farzamian et al., 2020; Hauck et al., 2002; Kasprzak, 2015). Recent advancements in ERT technology have led to the emergence of automated monitoring devices, such as the PROactive Infrastructure Monitoring and Evaluation (PRIME) system, successfully used for monitoring hydrogeological processes over space and time, including in remote and cold environments (Uhlemann et al.,



2021; Holmes et al., 2022; Cimpoiasu et al., 2023). Additionally, point sensors are used in combination with ERT
deployments in order to obtain in-situ calibrations between electrical resistivity and direct measurements of
moisture content (Garré et al., 2013).

115 In order to obtain a better understanding of moisture availability in soils at different stages of development since
deglaciation, as well as the variability of moisture across the landscape and seasons, we present a year-long
(summer 2021– summer 2022) time series of geophysical data obtained from two sensor array installations located
on the forefield of Midtre Lovénbreen, a retreating glacier in Spitsbergen (Svalbard). The dataset comprises
records of soil temperature, soil water content and snow depth, which complement 4D time-lapse images of
120 subsurface electrical resistivity. We describe patterns in the soil point sensor data regarding an anomalous spring
melt event and the spring freeze-thaw transition. We analyzed 4D ERT models in the context of local physical
and topographical conditions in order to quantify the location, direction and rate of progress of the spring thaw
front and used unsupervised automated clustering in order to classify regions of the subsurface more susceptible
to liquid moisture content change, a known driver for soil biological activity.

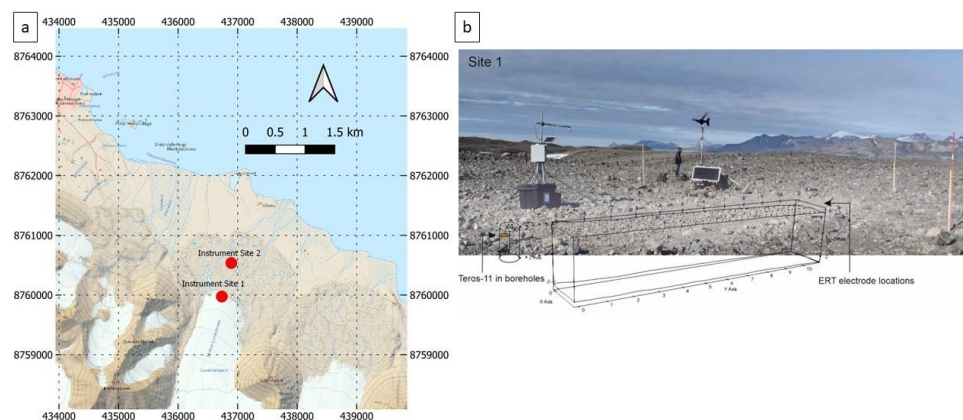
125 2 Methodology

2.1 Study sites

Midtre Lovénbreen (ML) is a polythermal non-surge-type valley glacier (Hambrey et al., 1999) with a north-
facing catchment located on the island of Spitsbergen, Svalbard Archipelago (Fig. 1a), approximately 5 km SE of
Ny-Ålesund (78°53' N, 11°59' E). The glacier has retreated approximately 1.5 km since its neoglacial maximum
130 attained in 1890 (Hambrey, 1894), uncovering a succession of sediments in different stages of development since
deglaciation (“chronosequence”). We selected two sites across the glacier forefield based on the time elapsed
since deglaciation, reflecting soil ages of 10 and 50 years, respectively. Cimpoiasu et al. (2023) describe the
physical properties of the two sites in more detail. Site 1 sediments are found to be alkaline, with a low cation
exchange capacity, large vesicles and minerals trapped in a loam texture. Site 2 sediments, in comparison, contain
135 less silt, but more sand, and have a higher porosity, smaller minerals and vesicles.
Investigations of Site 1 (Cimpoiasu et al., 2023) showed a more homogeneous structure with higher moisture
availability and saturation. Site 2 has revealed a stratified structure with higher moisture variability, potentially
explained by greater hydraulic conductivity.

140 2.2 Point sensor measurements

At both locations we augered four ~ 15 cm diameter boreholes of approximately 1 m depth. In each borehole we
installed six Teros-11 sensors (24 in total per site). We did not use any liner and the boreholes were backfilled
with the sediment extracted during drilling. Overlooking the boreholes, a snow depth sensor was installed. All
sensors are attached to a Campbell Scientific CR1000X Datalogger, powered from a 210 Ah battery bank and
145 sustained by a 10 W solar panel. The Teros sensors record hourly data of soil volumetric water content (VWC)
and temperature. On each sensor towers (Fig. 1b) we also installed a Browning Recon Force Elite HP4 nature
camera, which take daily photographs of the site, from approximately 2 m height, to complement the snow depth
readings.



150 **Figure 1: (a) Topographic map of the study area (© NPI, 2023) (b) Photograph of Site 1 showing the instrumental set-up and the corresponding schematics of the underground sensor installation and the ERT investigation volume.**



2.3 Electrical resistivity tomography

155 At both locations we installed 222 stainless steel tubular electrodes (high surface area) arranged in 6 lines of 37
electrodes, with 30 cm inline and interline spacing. In the absence of accurate differential GPS positioning, the
location and height of the electrodes were recorded manually with a tape measure and laser level. The electrical
resistivity measurements are conducted with the PRIME system (Cimpoiasu et al., 2023), which is powered from
a 315 Ah battery bank. Battery charge is sustained during the summer months by a 150 W solar panel and during
160 the dark winter months by a 300 W wind turbine. One complete set of measurements took approximately four
hours and contains 12,300 datapoints distributed over a shallow subsurface volume of approximately $11 \times 1.5 \times 2$
 m^3 . In order to extend battery life for data collection in the event of a disruption to the power supply, we acquired
measurements at a rate of once every four days during the fall and winter months, when the ground is frozen, and
changes are minimal. This pattern was followed by more frequent daily measurements starting 1st April 2022 for
165 a greater temporal resolution over the anticipated snow melt period. For each individual measurement, four
electrodes are automatically selected by a pre-defined command sequence. As low injection currents and high
contact resistances between the electrodes were expected during the winter months (Hilbich et al., 2011; Doetsch
et al., 2015), we chose a Multiple Gradient electrode configuration for its spatial resolution properties and greater
signal-to-noise ratio (Dahlin and Zhou, 2006). The full dataset was filtered and temperature-corrected post-
acquisition using the processing workflow detailed in Cimpoiasu et al. (2023). Once pre-processed, the data were
170 inverted using a 4D algorithm implemented in the Res3DInvx64 software from Geotomo (Loke, 2017), as
described by Wilkinson et al. (2022).

2.4 Relationship between soil electrical resistivity and moisture content

According to Archie's law (Archie, 1942) the electrical resistivity ρ of soils can be expressed as:

$$175 \quad \rho = \rho_w a S^m \Phi^n, \quad (1)$$

where ρ_w is the resistivity of the pore fluid, a is the tortuosity factor, S is the saturation, Φ is the porosity and m
and n are empirical fitting parameters. Archie's Law is most applicable when the soil and rock matrix can be
180 assumed to be non-electrically conductive. The glacial till sediments in the ML forefield are silty with relatively
low clay content, justifying this assumption (Cimpoiasu et al., 2003).

We divided the ERT volume into three layers of equal thickness, each layer spanning the depth range of two of
the six point sensors in every borehole (0-33 cm, 33-66 cm, 66 cm-1m). For every ERT timestep we computed
the average electrical resistivity value of each layer and the average corresponding VWC over the day of ERT
185 recording. We then split the range of VWC values into 30 equal 0.01 size bins and computed for every bin the
average VWC and its corresponding average electrical resistivity. To these data we fitted Archie's relationship
using laboratory-derived porosity values (as listed in Cimpoiasu et al., 2023), an assumed pore fluid resistivity
value of 100 Ωm and estimated values of a , m and n as fitting parameters.

190 2.5 Movement of the thaw front

Analysing timelapse ERT records, we made the assumption that the onset of soil thaw can be identified by a steep
drop in electrical resistivity. This allowed us to set a threshold electrical resistivity value of 1,000 Ωm for Site 1
and 3,000 Ωm for Site 2. We used these values to track movements of the thawing front in three dimensions, by
counting and identifying the location (local Cartesian coordinates, where the origin [0, 0, 0] is one corner of the
195 ERT volume) of all ERT model cells with values below the estimated thresholds. We determined the location of
the cell centres by computing an average of the cell coordinates for every timestep, allowing us to calculate
distance, rate of progress (gradient of distance) and direction of movement of the thawing front.

2.6 k-means clustering

200 Unsupervised automated algorithms are useful for identifying patterns in large datasets (Berkhin, 2006). A
k-means clustering algorithm partitions n observations into k clusters, in which each observation belongs to the
cluster with the nearest mean (cluster centers) (Berkhin, 2006). This method has been proven to be effective in
geoelectrical data classification (Audebert et al., 2014; Giuseppe et al., 2014, 2018). As described by Delforge et
al. (2021), time-lapse ERT datasets can be classified after the Coefficient of Variance (CV) of every model cell,
205 expressed as:

$$CV = \sigma/\mu, \quad (2)$$



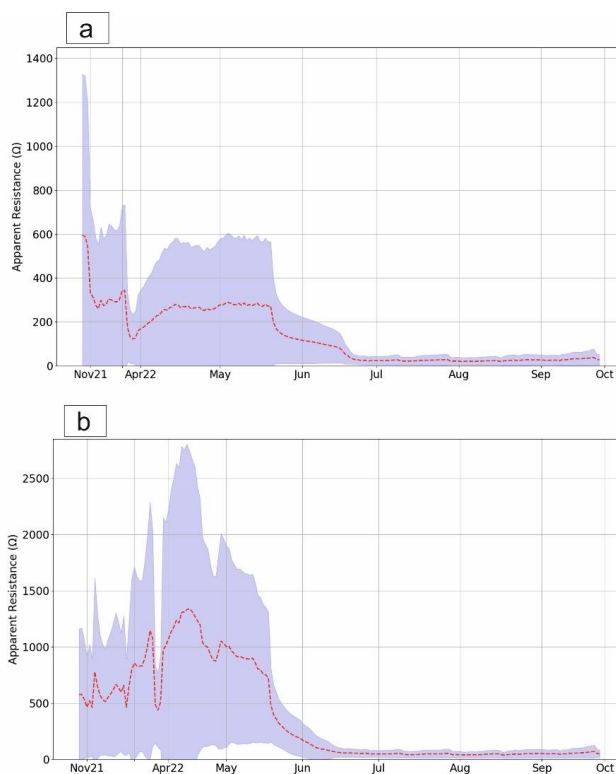
210 where σ and μ are the standard deviation and average, respectively, of electrical resistivity values associated with
a model cell. Firstly, an appropriate number of clusters was determined using the elbow method, where inertia
(sum of squared distance of samples to their closest cluster center) is plotted against the number of clusters and
the elbow of the obtained curve is selected as the number of clusters to use. Secondly, for every time step, we
computed the average resistivity values of all the cells within each cluster and the corresponding standard
deviation.

215

3 Results

3.1 4D ERT measurements

220 We have acquired 197 individual timesteps for Site 1 and 200 timesteps for Site 2. During strong winter storms
with high wind speeds, an overvoltage protection mechanism switched off the PRIME system during the
acquisition window on some occasions, resulting in several missing datasets during the winter months. The system
was subsequently reconfigured in March 2022, which should minimise this issue in the future.



225 **Figure 2: Evolution of apparent resistance (Ω) at (a) Site 1 and (b) Site 2. Red dotted line represents the mean apparent resistivity, and the shaded purple area represents the apparent resistance data distribution within one standard deviation.**

230 During the winter and spring months, we record high values ($>500 \Omega$ for Site 1 and $>1000 \Omega$ for Site 2) of apparent resistance (Fig. 2), with Site 2 showing higher overall values. Both sites record a drop in apparent resistance in mid-March followed by a steep recovery. Site 1 records its highest values (1300Ω) in late October 2021, whereas Site 2 records its highest values (2650Ω) in April 2022. In May 2022, Site 2 experienced a gradual decrease in resistance, whereas Site 1 experienced a two-step drop. Data standard deviation is lower when the average resistance is lower, with Site 2 showing larger overall standard deviations. Contact resistance values ranged



between 1-2 kW in the summer months and 50-60 kW during the winter. Due to high contact resistance values, data retention after filtering and quality control dropped from 97 % during the summer to 62 % during the winter (a complete metadata record is available upon request). Figure 3 shows a selection of inversion results for four ERT timesteps. Data for the first timestep was captured in February when the shallow subsurface is expected to be frozen. The images show elevated values of electrical resistivity at both sites. Site 2 exhibited higher and more uniformly distributed values. Strong positive changes in resistivity can indicate ice formation (in this case the reference dataset was acquired in the summer when the soil is expected to be unfrozen). The other three timesteps show a progressively thawing soil volume, indicated by the gradual drop in absolute resistivity values throughout the volume and the migration towards zero relative change.

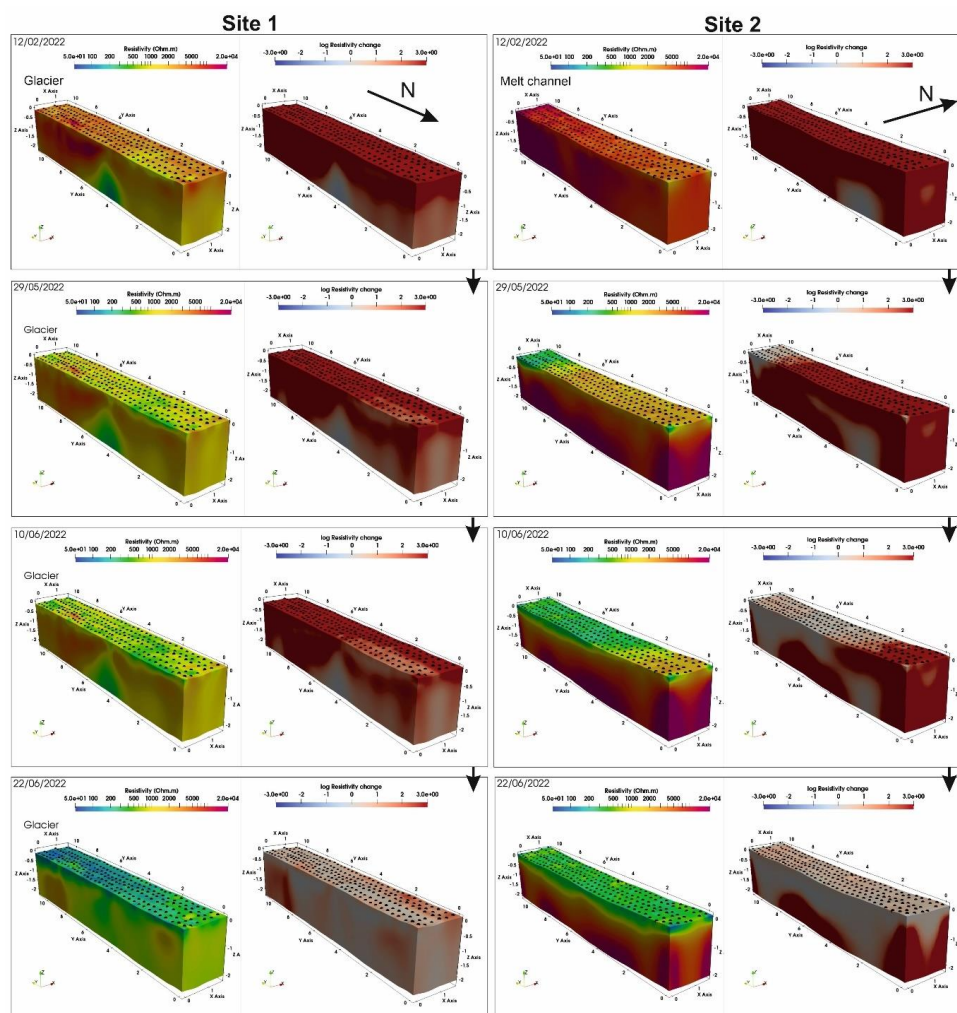


Figure 3: Inversion results for four selected ERT timesteps. A 3D model of absolute electrical resistivity values is shown on the left-hand side of the subplots and resistivity change relative to ERT data recorded on 2nd Aug 2021 on the right-hand side. Black dots on the surface of the models represent the position of the electrodes.

245 3.2 Point sensor measurements

Teros-11 sensors measured continuously from August 2021 to October 2022 (Fig. 4). Both sites experienced data loss due to battery failures. As a result, at Site 1 there are gaps in the data between 3rd Dec 2021 to 7th Mar 2022 and 25th May to 1st June, and at Site 2 between 30th Sep to 26th Oct and between 23rd Dec 2022 to 7th Mar 2022.



250 This meant that the soil freeze, occurring between 10th and 19th of October 2021, could not be captured at Site 2 during this time interval.

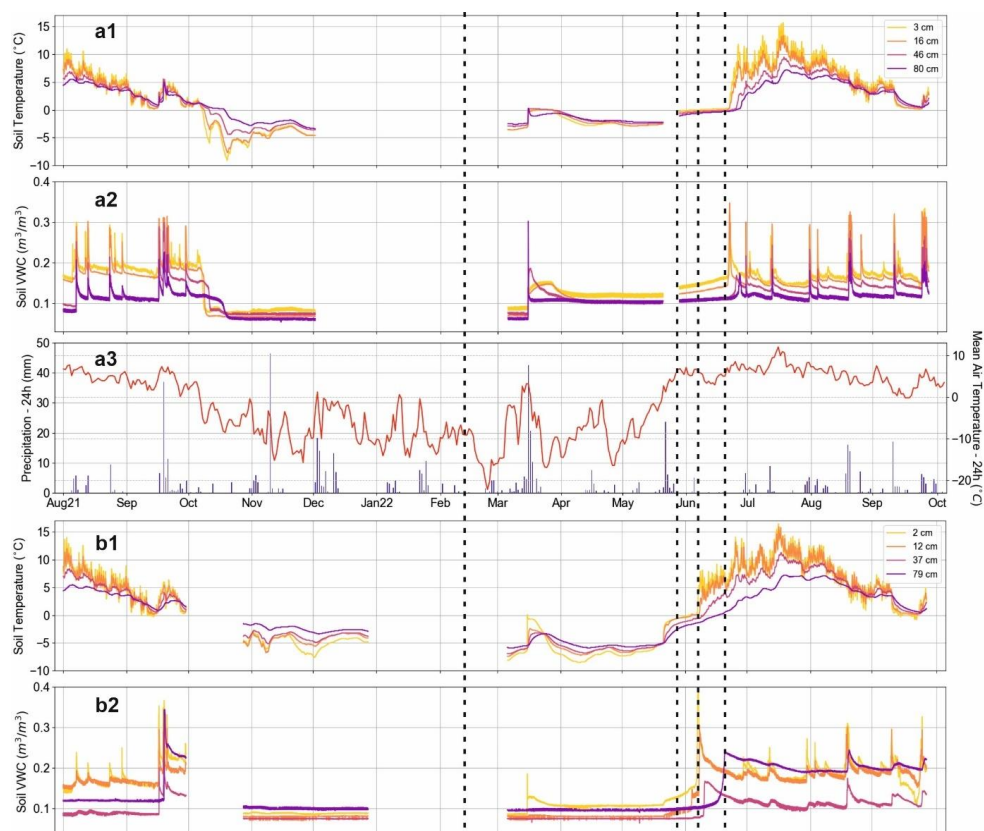


Figure 4: Point sensor data from Sites 1 and 2 showing soil temperature (a1, b1) and soil VWC (a2, b2) between Aug 2021 and Oct 2022, together with air temperature and precipitation (a3) recorded by the Ny-Ålesund weather station (Seklima, 2023). Dotted lines mark the four ERT timesteps shown in Fig. 1.

255 Soil thawing occurs at each site when soil temperature rises above 0°C. This is confirmed by a steep increase in VWC values as more liquid water becomes available. According to weather records (Fig. 4 a3), air temperature consistently stays above 0°C starting 17th of May 2022, but this date does not coincide with the soil freeze-thaw transition at either of the sites, even though soil temperature at Site 2 concurrently starts to increase (records unavailable at Site 1). At both sites, thaw onset occurs earlier in the year for the layers closer to the ground surface.

260 Soil temperature decreases with depth at both sites, with Site 2 warmer in the summer months, and Site 1 generally warmer in the winter months. During the summer months, daily variations in temperature are visible in the uppermost two layers and are seemingly attenuated with depth. September 2021 VWC levels are generally similar to summer 2022 levels. VWC spikes during the summer months coincide with large values in the precipitation record. Site 1 sees larger VWC spikes than Site 2 during such events. VWC at Site 2 in the uppermost two layers is generally higher than at Site 1 in 2022.

265

Both stations have captured an anomalous event in mid-Spring 2022 (Fig. 5), manifested by a sudden increase in soil temperature and VWC, confirmed in the weather records with sustained air temperatures above 0°C for approximately four days and 85 mm of precipitation over the whole week (11th Mar – 18th Mar), with a maximum of 40 mm recorded on the 15th of March. At Site 1 soil temperature has reached 0 °C at all depths monitored, coinciding with a spike in the VWC recordings. Once the event ended and the temperature dropped below 0 °C,

270



values of VWC were higher than before the event at all depths. At Site 2 only the shallowest sensor detected a soil temperature above 0 °C during the event, which also caused a spike in VWC values at this depth.

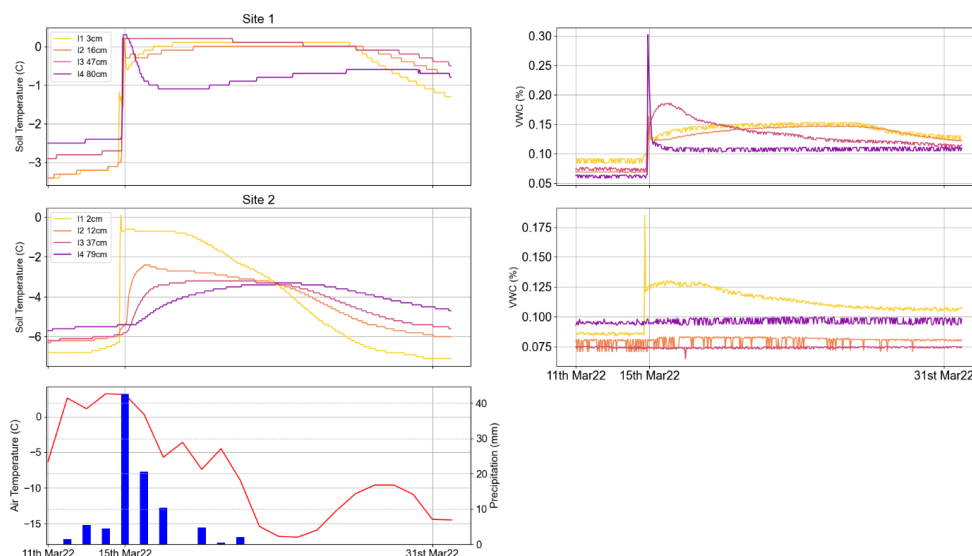
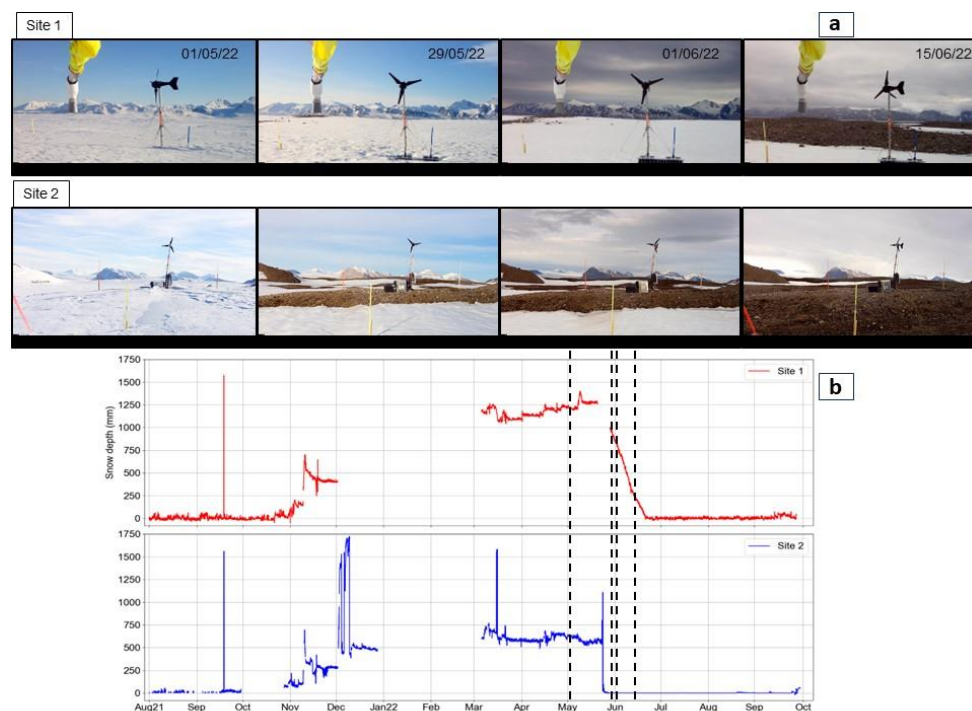


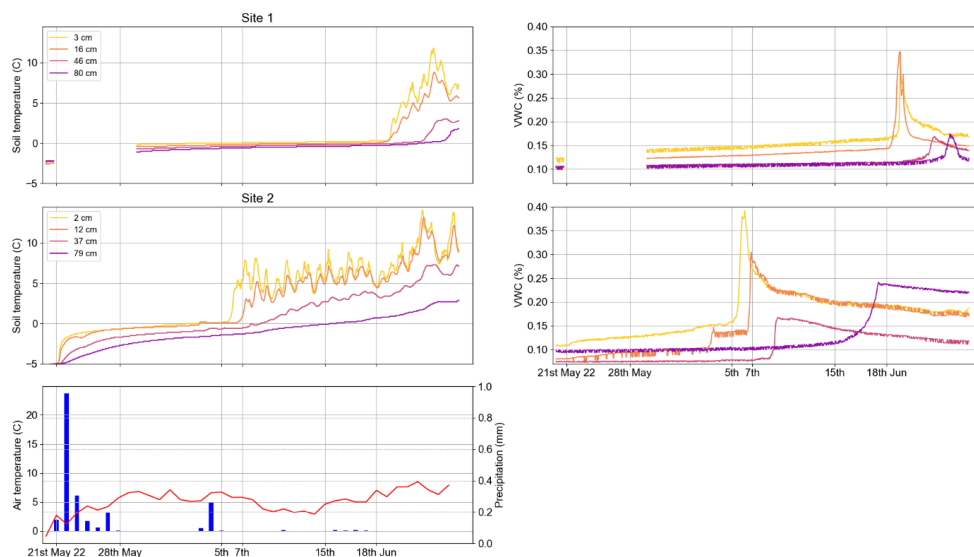
Figure 5: Soil temperature and soil VWC at Sites 1 and 2 during the mid-March thaw event, shown together with corresponding air temperature and precipitation records (Seklíma, 2023).



275 Figure 6: (a) Nature camera photographs of the two sites. (b) Snow depth measurements corresponding to Sites 1 and 2. Dotted lines in B indicate the dates the photographs were taken.



We present the freeze-thaw transition above ground in greater detail (Fig. 6), as photographs obtained by the nature cameras display the gradual reduction in snow cover. This visual observation is confirmed above ground by direct measurements of snow depth, and below ground by the buried point sensors (Fig. 7). We recorded a snow depth of 1,250 mm when the snowpack was at its maximum at Site 1 and approximately 600 mm at Site 2. We also observed a faster reduction of snowpack thickness at Site 2 after the air temperatures rose above 0 °C and a 13-day delay in soil thaw between sites, indicated by steep spikes in soil temperature and VWC values. By contrast, Site 1 shows a more gradual reduction in snow cover. VWC increases due to the freeze-thaw transition occurring on different dates for different soil layers. There is a larger delay between layers at Site 2 as compared to Site 1, with the largest delay of seven days recorded between 37 and 79 cm at Site 2. VWC values spike once the soil temperature rises above 0 °C. At Site 1 we observe greater VWC spikes of 0.15-0.2 recorded by the top two sensors, compared to the ones recorded by the bottom two sensors of only 0.05. Shortly afterwards (approximately one day), the VWC values revert to values 0.02-0.03 higher than prior to thaw. At Site 2 we observe similar 0.15-0.2 spikes in VWC for the top two sensors, but slightly higher values for the bottom sensors

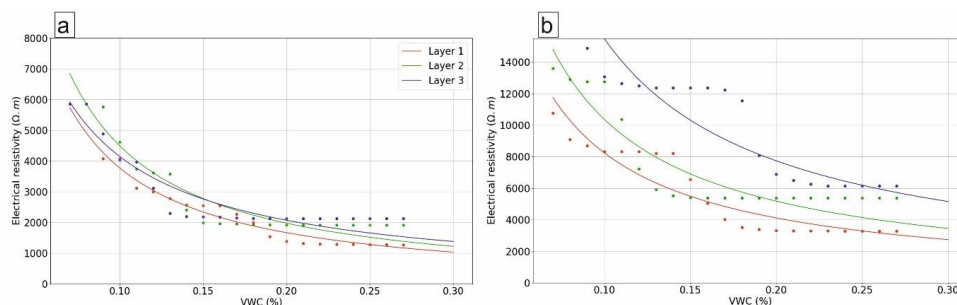


of 0.07 and 0.18, respectively. After the thaw transition, the decrease in VWC is much slower than at Site 1, taking up to two weeks to record constant values of VWC. Furthermore, the VWC values post-thaw are higher than the ones recorded before, 0.08 for the top three sensors and 0.12 for the deepest sensor.

Figure 7: Soil temperature and soil VWC at Sites 1 and 2 during the late May–mid June freeze-thaw transition, together with corresponding air temperature and precipitation records (Seklima, 2023).

3.3 Relationship between electrical resistivity and moisture content

Figure 8 shows the relationship between ER and VWC based on in-situ measurements. Archie’s law was fitted with the following parameters: Site 1 layer 1 ($a=0.36$, $m=2.10$, $n=2.34$), Site 1 layer 2 ($a=0.32$, $m=1.95$, $n=2.58$), Site 1 layer 3 ($a=0.28$, $m=1.85$, $n=2.59$), Site 2 layer 1 ($a=0.55$, $m=2.65$, $n=1$), Site 2 layer 2 ($a=0.58$, $m=2.76$, $n=1$), Site 2 layer 3 ($a=0.64$, $m=2.94$, $n=1$). VWC recordings range between 0.07 and 0.27. Only for Site 2 layer 3 we notice a narrower range of 0.09-0.27. At Site 1 the Archie curves for different layers have similar shapes. The uppermost layer shows less resistive values when compared to layers 2 and 3, which exhibit a very similar distribution. The calibrated Archie curve misfit is generally low (p-values for layers 1-3: 0.56, 0.62, 0.52), albeit slightly underestimating resistivity values in layers 2 and 3 at high VWCs. Site 2 appears more resistive than Site 1 at equivalent values of VWC. Furthermore, Site 2 shows Archie curves with distinct differences between layers, with values of resistivity increasing with depth throughout the VWC range. The curve does not fit the data as well as for Site 1 (p-values for layers 1-3: 0.60, 0.46, 0.73), with measurement values in the range 0.14-0.18 not following the Archie model (Laloy et al., 2011).



310 **Figure 8: Best fit of Archie's law (curves) to in-situ measurements of electrical resistivity and soil VWC (dots). (a) Site 1 layers 1-3, (b) Site 2 layers 1-3.**

3.4 Thawing front progression

315 Figure 9 presents a visualisation of the thawing front progression at the two sites. The ERT models appear truncated because cells with resistivity values above at chosen thresholds are masked. As time progresses, the visible cells have lower resistivity values and new cells emerge, as their resistivities fall below the selected threshold. At Site 2 we observe a clear progression of the thawing front from NE to SW. At Site 1 the progression of the thawing front is not as evident in the timeframe selected as at Site 2, although the emergence of new cells can also be observed.

320 The spatial progression of the thaw front is shown in Fig. 10. The Cartesian coordinates (Fig. 10 a2-a4, b2-b4) of the cell centre define the direction of the front. At Site 2 the movement of the cell centre starts in late May, marked by a steep movement in the Y direction (along the length of the model) at a rate of up to 1 m/day at its peak (Fig. 10 b1 and b3), and in the Z direction (in depth) at a rate of up to 0.02 m/day (Fig. 10 b4). Towards the end of the monitoring period, the cell centre tends towards the centre of the model (0.75 m in X , 5.5 m in Y and 0.5 m in Z) as all the cells have now passed the thaw threshold. For Site 1 we observe two periods of movement; the first concurrent with the movement detected at Site 2, and the second observed in the second half of June. Gradient measurements (Fig. 10 b2-b4) indicate that during the first period of displacement the cell centre has moved at a greater rate (up to 0.059 m/day in X , 0.41 m/day in Y , 0.073 m/day in Z) than during the second period (0.018 m/day in X , 0.1 m/day in Z , 0.04 m/day in Z). In the Z direction (Fig. 10 a4 and b4), the cell centre has moved up during the first period of movement and down during the second period. Figure 10 a1 shows thaw cell proportion over time across different layers and the whole model volume. Towards the end of the monitoring window, during the summer when all cells should be below the threshold, the thaw cell proportion is at 100%. At the beginning of the monitoring window, the proportion is not at 0% for all layers shown because some of the model cells had lower resistivities pre-thaw. Site 1, despite seeing a delayed cell proportion increase, reaches 100% proportion before Site 2, which has an initial fast increase phase, followed by a slower gradual increase in the second half of June. Cell proportion dips below 100% in July at Site 1 only to recover towards the end of the month. Surface layers (numbered 1 in Fig. 10) show a faster increase in thaw cell proportion, with Site 2 layer 1 the fastest. By contrast, the deepest layers (numbered 3 in Fig. 10) show a slower increase, with Site 1 layer 3 the slowest.

325
330
335

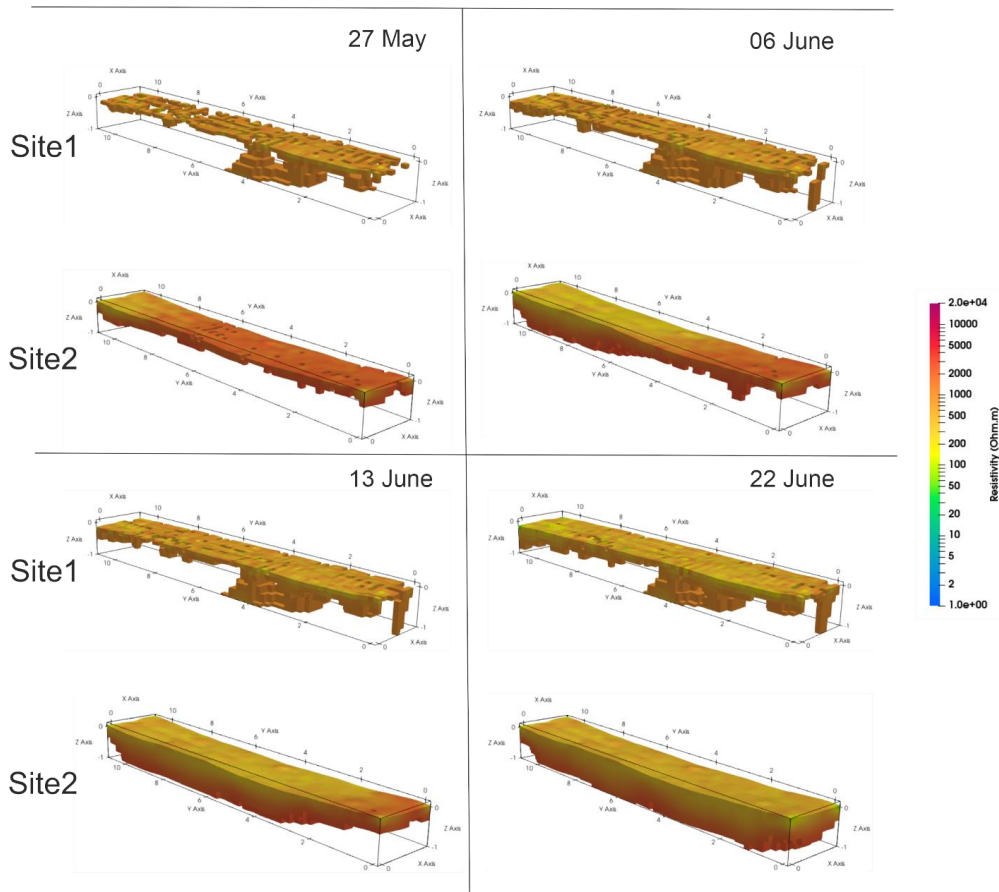


Figure 9: Four selected ERT timesteps showing only model cells with resistivities below the site-specific thaw threshold values.

340

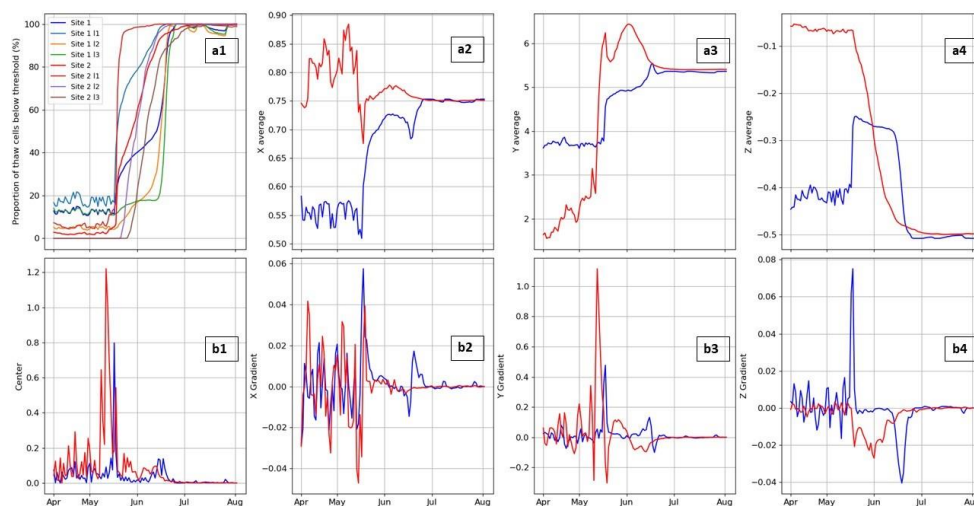


Figure 10: Thaw cells distribution across the ERT volume. (a1) Number of thaw cells as proportion of the ERT volume and the three layers of equal thickness described in 2.4. (a2) X Coordinate (a3), Y Coordinate and (a4) Z Coordinate of the thaw cells' centre. (b1) Movement distance of the thaw cells' centre. (b2) Movement gradient in X, (b3) Y and (b4) Z direction of the model cells' centre.

345

3.5 k-means clustering

The coefficient of variance (*CV*) distribution within the ERT volume space is shown for both sites in Fig. 11. There are overall higher values of CV at Site 2 than at Site 1, with very high values (>2) at the edge of the model. There are generally higher CV values within the first meter below the model surface at both sites. However, Site 2 shows higher values in some regions below 1 m depth. At Site 1 the median CV value is 0.78 and at Site 2 it is approximately 1. For Site 1, all model cell values are within two standard deviations from the median, whereas for Site 2 there are several model cell values outside this range.

350

Three clusters have been determined as optimal for the existing datasets (Fig. 12 a3). The spatial division of the model cells by corresponding cluster is shown in Fig. 12 a1, a2. For Site 1, clusters 1 and 3 show similar average resistivity values over time during the winter, whereas cluster 2 shows resistivity values that are lower in comparison. However, post-thaw, during the summer months, all clusters had similar values. Cluster 3 shows the highest values of standard deviation and cluster 2 the lowest. Values of standard deviation are higher during the winter months for all clusters. All clusters also show a similar drop rate in resistivity when soil thaw begins at Site 1 in mid-June. This continues until the last week of June 2022. Furthermore, all clusters show a dip in resistivity during March 2022, coinciding with the anomalous warm event. For Site 2, all clusters show comparatively higher values of average resistivity and standard deviation than the Site 1 clusters during the winter months, with cluster 2 registering the highest values. A drop in average resistivity values in all clusters marks the onset of soil thaw in late May 2022. The drop has a lower rate than at Site 1 and lasts comparatively longer until the first week of July 2022. After thaw onset, cluster 3 shows the highest standard deviation values. Finally, similarly to Site 1, we find a dip in average resistivity values in March 2022.

365

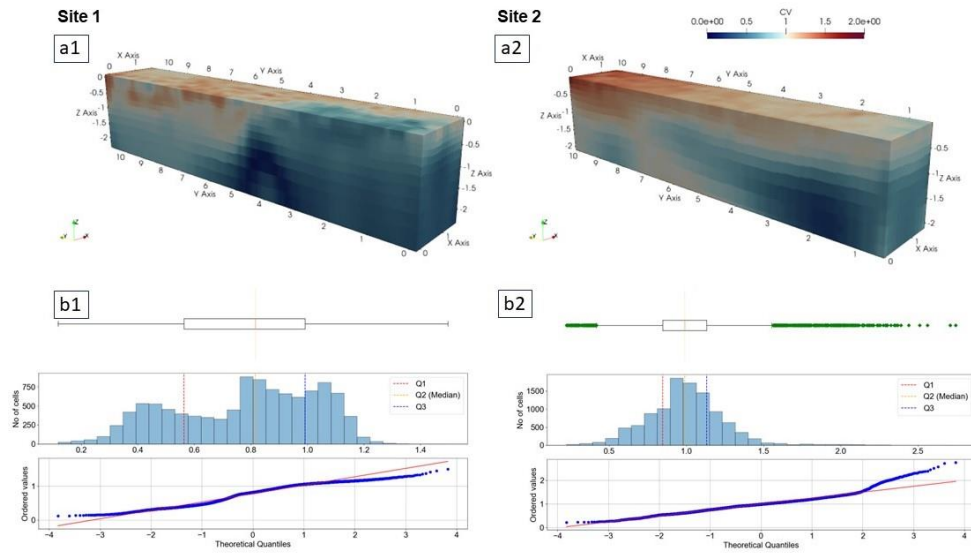
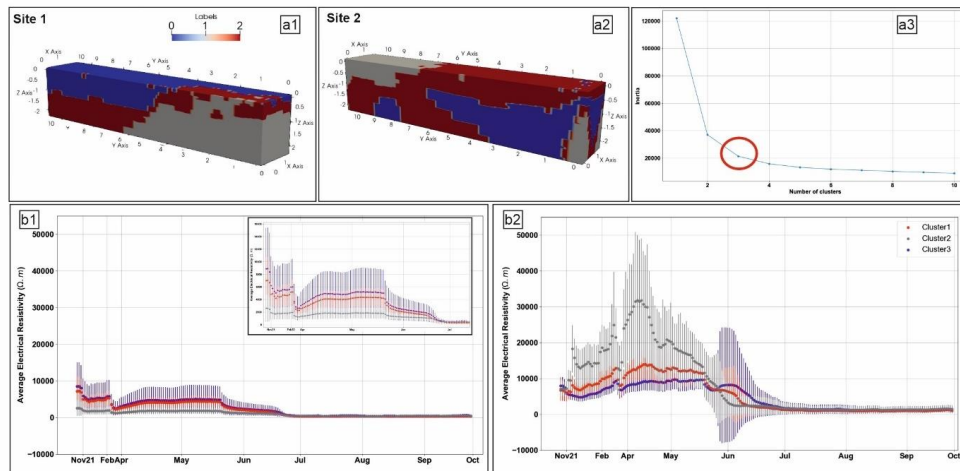


Figure 11: Spatial distribution of CV values corresponding to (a1) Site 1 and (a2) Site 2. Boxplot, histogram distribution and quantile-quantile plot with respective quartiles of CV values corresponding to (b1) Site 1 and (b2) Site 2.



370 Figure 12: Spatial cluster division of ERT model cells in reference to their CV value corresponding to (a1) Site 1 and
 (a2) Site 2. (a3) Results of the elbow method with the chosen number of clusters highlighted by the red circle. Average
 resistivity and standard deviation values recorded between November 2021 and October 2022 corresponding to (b1)
 Site 1 and (b2) Site 2 clusters.

4. Discussion

375 4.1 Anomalous snowmelt event

The detection of the snowmelt event in mid-March 2022 presents us with the opportunity to analyze the conditions
 that enabled its occurrence. There were several other instances when air temperature increased above 0 °C (e.g.
 December 5th 2021), but there was minimal observed impact on soil temperature or ice content. However, the
 duration of these events was much shorter than what was recorded in March, when 96 hours of sustained air
 temperatures above 0 °C caused snowmelt, which occurred during a time of elevated precipitation. Consequently,
 380 melt water infiltrated sediment layers, and we observed an increase in soil temperature and liquid water content.



At Site 1, the top 60 cm of the subsurface was maintained at around 0 °C temperature for almost a week, even after air temperatures dropped below freezing. Furthermore, the liquid water content levels of the sediments remained elevated for the rest of the spring. This has direct consequences on soil biological activity, carbon and nutrient cycling (Brooks et al., 1997; Schmidt et al., 2009).

4.2 Soil freeze-thaw transition

Point sensor loggers recorded an extensive dataset over a full yearly cycle, capturing the freeze-to-thaw transition of the sediments present at both study sites. As proposed in Cimpoiasu et al. (2023), proximity to the glacier and local topography is responsible for different thermal gradients and precipitation influxes between sites. This is corroborated by higher soil temperatures at Site 2 and greater VWC spikes at Site 1 during the summer months. Variations in snow accumulation and rate of snowmelt are further evidence of the differences in thermal gradient and precipitation influx between sites. Site 1 experienced greater snow depths and a longer period of snow cover than Site 2, likely driven by generally lower air temperatures at Site 1 that are regulated by the presence of the glacier and the flat topography, which promotes snow accumulation. A prolonged snow cover implies prolonged thermal insulation for underlying sediments, which then led to a delayed freeze-thaw transition at Site 1. This is consistent with the argument put forward by Zhang et al. (2005) that seasonal snow cover can result in an increase of the mean annual ground surface temperature by several degrees and can substantially reduce the seasonal freezing depth.

An additional 13 days with temperatures below freezing may impose limitations to soil biological activity, and therefore impede the rate of soil development. However, point sensors detected an increase in soil temperature and VWC under the snowpack even before its melt. This implies that a fraction of the frozen pore water in the sediment transitioned into liquid phase even before the ground surface was completely exposed. Soil biological activity may occur when liquid water is present, even in pore water – and therefore may persist for a period of 29 days at Site 1 and 15 days at Site 2, respectively, whilst soils remain at temperatures below 0 °C.

We observed an intermediate period during the soil freeze-thaw transition when the soil temperature stayed around the 0 °C isotherm (Fig. 7), occurring at Site 1 between 28th May–19th June (23 days) and at Site 2 between 1st June–6th June (6 days). This phenomenon is known as the zero-curtain effect and, in this case, occurs when the soil water phase transition to liquid is slowed down by the release of latent heat from the soil to the snowpack (Zhang, 2005). On this basis, a thicker snow layer at Site 1 likely extended the zero-curtain period. According to Elberling and Brandt (2003), microbial activity may continue in unfrozen soils whilst the diffusion and advection of the produced CO₂ may be obstructed by the freezing fronts and overlying snowpack. Similar zero-curtain patterns have been observed in the soil temperature data recorded by Boike et al. (2018) at a location a few kilometers north-west from our sites.

4.3 Spatial and temporal behaviour of electrical resistivity

As shown in Fig. 1, electrical resistivity closely followed the events and patterns observed in the point sensor data. This is to be expected, given that electrical resistivity is strongly influenced by liquid water availability (Samouëlian et al., 2005). Throughout the year, we captured higher electrical resistivity values at Site 2. The location is warmer and drier during the summer months and colder during the winter months, which would imply less available liquid water for electrical conduction; this is due to a larger proportion of the pore space being air-filled during the summer and ice-filled during the winter.

Four dimensional ERT enables us to track electrical resistivity changes spatially and temporally over the study volume. The resulting models corresponding to both sites contain regions that experience only marginal resistivity changes throughout the year. According to Irvine-Flynn et al. (2011), this could be explained by the presence of buried ice or large boulders within the matrix of the glacial diamicton and reworked sediments, both of which would be less susceptible to fluctuations in temperature and VWC. Edges and corners of the ERT models show anomalously high values of resistivity, which is especially apparent at Site 2 (Fig. 3, 29/05 and 10/06). This can be explained by poorer sensitivity of the sensor array to those regions, with data cover being more limited towards the outer edges of the model.

As the sediments thawed, we observe changes in electrical resistivity throughout the respective 3D image volumes recorded at these timepoints. At Site 2 in the top 40 cm, a distinctive layer of low resistivity forms and extends throughout the volume as time progresses, whereas at Site 1 changes are more uniform. A physically distinct surface layer could be the result of extensive weathering and redeposition of the periglacial deposits, as Site 2 sediments have been exposed approximately 40-45 years longer than the ones found at Site 1.



435 Archie's law enables us to formulate a site-specific relationship between the electrical resistivity of the observed
sediments and their moisture content. We obtained similar relationships with good data fits for the three layers
present at Site 1, which is further corroborating evidence for its greater spatial homogeneity. Relationships
corresponding to layers 2 and 3 underestimate the resistivity values associated with higher values of moisture
content. This is because we had very limited data at that end of the VWC range, with VWC values above 0.2 only
440 recorded during brief summer precipitation events with little impact on the average resistivity of a sediment layer,
especially at depth. Archie relationships at Site 2 show a comparatively worse fit due to a data gap during the
October 2021 freeze, which could have provided thaw-freeze transitional values of moisture content. Overall,
older sediments show greater sensitivity of electrical properties to changes in VWC, which suggests that they dry
and freeze faster, shortening the transitional period for microbiological activity within them.

4.4 Tracking the thaw front

445 Throughout the winter months, a certain proportion of ice to liquid water content is maintained at a constant level
in the pore space throughout the monitored soil volume, as shown by the point measurements of VWC. By
attributing a bulk electrical resistivity value to such a constant proportion in the soil volume, we established a
numerical threshold between what can be considered sediments under frozen conditions and sediments undergoing
thaw, which will exhibit electrical resistivities below the threshold value. The appearance of new cells in the Fig.
450 9 timesteps visualises the progression of the thaw front at both sites. Several snow-soil interface cells in the
shallow layer (top 20 cm) have electrical resistivity values below the threshold, even before the nominal date
when soil temperature rises above freezing. On 6th June at Site 2, we observed that the thaw front had progressed
at depth and it continued laterally over the following days. However, at Site 1 we did not observe the same effect;
rather the first signs of depth propagation can be seen in the 22nd June timestep, concurrent with point sensor
455 records that mark the first soil temperature above freezing on the 19th June.

Despite commencing later than at Site 2, the thaw at Site 1 covers the entire imaged volume first, as shown in Fig.
10 a1. This can be explained by a greater quantity of snowmelt, which infiltrated into the soil and lowered the
bulk electrical resistivity of the shallow subsurface. Furthermore, the flat topography of Site 1 suggests that a
greater proportion of the snowmelt will infiltrate the soil rather than generating surface run-off redirected into
460 melt channels. The latter is more likely to occur at Site 2, driven by its hummocky topography.

The Site 1 thaw progression shows two stages of movement; first in mid-May, coinciding with the rise of air
temperature above freezing, and then in mid-June when the snow cover disappeared. Between the two stages, the
zero-curtain effect maintained the temperature of the shallow subsurface around 0 °C with minimal changes to
electrical resistivity. A positive cell centre gradient in Z (Fig. 10 b4) indicates that changes in the first stage of
465 thaw happened at the surface of the monitored volume, followed by a negative change, indicating propagation of
thaw vertically downwards. The latter is faster than what we observed at Site 2 (4 cm/day versus 2 cm/day,
respectively), illustrating the meltwater infiltration effect discussed above.

Despite being covered by a thinner layer of snow, Site 2 showed generally a faster movement of the thaw front,
with the cell center moving by up to 120 cm in one day. However, the movement was primarily lateral (largest
470 gradient values seen in the Y-direction – Fig. 10 b2-4) along the length of the monitored volume. This highlights
the directionality of the snowmelt, which progressed towards the melt channel located at the far end of the
electrode array (Fig. 3). Layers 2 and 3 changed more slowly compared with the surface layer (Fig. 10 a1), and
the deepest layer (>70 cm) experienced a reduction in gradient only once all the overlying snow had melted in
mid-June. These observations strongly suggest that thaw in the near subsurface is driven primarily by meltwater.
475 Therefore, factors such as topography and snow thickness need to be taken into account when investigating the
timing of soil biological activity, particularly at depth. Yi et al. (2015) drew a similar conclusion, as their model
results showed that increased snow cover promotes soil respiration at depth.

4.5 CV and unsupervised clustering

Coefficients of Variance at Site 2 were generally greater than at Site 1 (Fig. 11 b2). Values outside two standard
480 deviations correspond to cells at the edge of the model, where due to reduced sensitivity electrical resistivity
change is overestimated. Regions in both models with very low CV are likely indicating the location of buried
boulders or ice, which did not see significant change over the monitoring period. The histogram and quantile-
quantile plot in Fig. 11 show a normal distribution at Site 2, whereas those at Site 1 exhibit a more uniform
distribution, implying that the younger sediments have a wider range of electrical resistivity variance values. At
485 both sites we notice CV outlier values, towards the high end of the spectrum, manifested by strong deviations
from the 1:1 quantile line. The retreating glacier uncovered a mixture of silty and sandy sediments, along with



490 gravels and boulders. Subsurface volumes with varying proportions of sediment to boulders will exhibit different water storage capacities and hence different variance of electrical resistivity. At Site 2 we found more aggregated sediments with smaller and fewer boulders present, resulting from years of erosion. This generates a more uniform spatial change in electrical resistivity (Cimpoiasu et al., 2023).

495 K-means clustering divided the two monitored volumes into three clusters (Fig. 12 a1-2). The clusters appeared to be localized and did not extend over the entire length or depth of the model. All clusters had large standard deviations during the winter months due to poor data quality, explained by very high contact resistances (~50 k Ω) between the electrodes and the frozen ground, which allowed only very small currents (0.5 mA) to be injected for each measurement. Site 1 Cluster 3 cells were likely clustered due to the increased moisture content in that region of the model, with the lowest values of electrical resistivity observed during the summer months and the highest during the winter months. Site 1 Cluster 2 represents the region with the smallest change. Site 1 Cluster 1 appears to group cells with intermediate values of CV, however it appears to be a close extension of Cluster 3, given the similarity in average resistivity values. Site 2 Cluster 2 contains cells with the highest values of CV, average resistivity and standard deviation. This far end of the model is in closer proximity to the melt channel and experienced the highest fluctuation during freeze-thaw transitions. The standard deviation in Site 2 Cluster 3 increased right after the spring melt onset, with a peak at the beginning of June, directly correlated with the flow of meltwater perturbing the recordings of electrical resistivity. Site 1 Cluster 3 is the cluster with the largest number of cells, grouping the cells with median values of CV (Fig. 11 b2).

505 The clustering algorithm provides an unsupervised method of selecting regions of the model that are more or less dynamic. In our context, it identifies the regions most affected by meltwater infiltration and the regions which are less likely to change. Older sediments show similar CV values within Cluster 1 across all depths of the model. This implies that seasonal water availability regimes are similar across this region, and although concentrated in the top 1 m of sediment, soil biological activity can potentially extend down to 2 m in depth.

510 **Conclusions**

In this study we use an ERT monitoring system complemented by point sensors in order to monitor deglaciated soil temperature, moisture content and electrical resistivity across one calendar year (Aug 2021–Aug 2022). We installed two sensor stations on the forefield of Midtre Lovénbreen, a retreating glacier located on Spitsbergen, Svalbard archipelago, overlaying sediments deglaciated approximately 10 and 50 years ago respectively. We established subsurface layer specific Archie's law-based pedophysical relationships between co-located measurements of electrical resistivity and moisture content. Continuous sensor records allowed us to characterize an anomalous snow melt event that elevated the soil liquid water content at the younger site for the remainder of the Arctic spring, with potential consequences for soil biological activity under the snowpack. We obtained almost uninterrupted ERT recordings, which revealed unprecedented 4D images of the Arctic soil freeze-thaw transition. 520 Furthermore, this enabled us to calculate the speed, direction, and magnitude of the thawing front, and compare them across the two sites. Strongly shaped by topography and snow thickness, at its peak, older sediments had a lateral thaw propagation of 1 m/day, whereas the younger sediments exhibited a vertical thaw propagation of 0.4 m/day. During the shoulder period between freeze and thaw, older sediments experienced the zero-curtain effect, which maintained temperatures around the 0 °C isotherm for six continuous days, whereas the younger site experienced it for 23 days. During this time, the soil microbial communities are potentially active under the snowpack. Finally, unsupervised clustering helped to classify regions of the imaged sediment volume according to their electrical resistivity coefficient of variance, which allowed us to identify regions more or less susceptible to changes in their water content. Older sediments showed similar variability across the profile down to 1 m below the surface, indicating an increased likelihood for microbial activity at depth.

530 Together, these results illustrate how physicochemical characteristics and freeze-thaw dynamics, potentially driven by topography and alterations due to weathering, develop the Arctic sediments over the first several decades after being exposed by glacier retreat. The length of the zero-degree curtain, instances of large melt events, and heterogeneity of soil freezing all have implications for the soil biological activity that is enabled by liquid water, and thus the carbon dynamics of newly exposed soils. As air temperatures and precipitation continue to increase in the High Arctic, leading to further ice loss and exposing more underlying sediments, further research on continuous freeze-thaw dynamics in three-dimensional volumes of soil will be important to better constrain the impacts of the newly exposed landscapes on global carbon fluxes.



540 **Author contribution**

MOC - Responsible with fieldwork planning, field installation (BGS PRIME), data acquisition, data processing and manuscript writing. OK - Responsible with project management (co-PI), fieldwork planning and manuscript editing. HH - Responsible with fieldwork planning, field installation (BGS PRIME), data acquisition and manuscript editing. PBW - Responsible with initial system design (BGS PRIME), data processing (BGS PRIME) and manuscript editing. PM - Responsible with initial system design (BGS PRIME) and fieldwork planning. JEC – Responsible with fieldwork planning, data interpretation and manuscript editing. DL - Responsible with fieldwork planning, field installation, data acquisition and instrument maintenance (University of Utah point sensors). CO - Responsible with project management (co-PI), initial system design (University of Utah point sensors), fieldwork planning and instrument maintenance. SKS - Responsible with project management (co-PI), fieldwork planning and field installation. PS - Responsible with project management (co-PI), fieldwork planning, field installation and manuscript editing. TPI - Responsible with project management (co-PI), fieldwork planning, field installation and manuscript editing. ZL - Responsible with instrument maintenance. AS – Responsible with instrument maintenance and manuscript editing. JAB - Responsible with project management (co-PI), fieldwork planning, field installation and manuscript editing.

555 **Data availability**

Data is available upon request.

Competing interests

The authors declare they have no conflict of interests.

Acknowledgements

560 This work was funded by the NSF-UKRI Signals in the Soil program (award numbers, NERC: NE/T010967/1, NE/T010568/1; NSF: 1935651, 2015329, 1935689), and also received financial support from the NERC Covid fund (administered by the British Antarctic Survey). Our work also benefited from Trans-National Access support (project AMBER-ICE) from the European Union's Horizon 2020 project INTERACT, under grant agreement No. 730938 to JB, and the CNRS Chaires de Professeur Junior (CPJ) to JB. We thank the UK NERC Arctic Research Station and the Norwegian Polar Institute Sverdrup Station in Ny-Ålesund, Svalbard, as well as Kings Bay Research for sharing their extensive local knowledge and logistical support. We would also like to thank Juan Carlos Trejos, Justin Byington and Michael Jarzin Jr. for assistance and logistical support in the field. The paper is published with the permission of the Executive Director, British Geological Survey (UKRI-NERC).

References

- 570 Archie, G.E.: The electrical resistivity log as an aid in determining some reservoir characteristics. Transactions of the American Institute of Mining, Metallurgical and petroleum Engineers, 146, 54–62, 1942.
- Arndt, K.A., Lipson, D.A., Hashemi, J., Oechel, W.C. and Zona, D.: Snow melt stimulates ecosystem respiration in Arctic ecosystems. *Global Change Biology*, 26(9), pp.5042-5051, 2020.
- 575 Audebert, M., Clément, R., Touze-Foltz, N., Günther, T., Moreau, S., Duquenois, C.: Time-lapse ERT interpretation methodology for leachate injection monitoring based on multiple inversions and a clustering strategy (MICS). *J. Appl. Geophys.*, 111, 320–333. <https://doi.org/10.1016/j.jappgeo.2014.09.024>, 2014.
- 580 Berkhin, P.: A survey of clustering data mining techniques. *Grouping Multidimensional Data*. Springer-Verlag, pp. 25–71, https://doi.org/10.1007/3-540-28349-8_2, 2006.
- Boike, Julia; Nitzbon, Jan; Anders, Katharina; Grigoriev, Mikhail N; Bolshiyarov, Dmitry Yu; Langer, Moritz; Lange, Stephan; Bornemann, Niko; Morgenstern, Anne; Schreiber, Peter; Wille, Christian; Chadburn, Sarah; Gouttevin, Isabelle; Burke, Eleanor J; Kutzbach, Lars: A 16-year record (2002–2017) of permafrost, active-layer, and meteorological conditions at the Samoylov Island Arctic permafrost research site, Lena River delta, northern Siberia: an opportunity to validate remote-sensing data and land surface, snow, and permafrost models, *Earth System Science Data*, 11(1), 261–299, <https://doi.org/10.5194/essd-11-261-2019>, 2019.



- 590 Bradley James A., Singarayer Joy S. and Anesio Alexandre M.: Microbial community dynamics in the forefield
of glaciers. *Proc. R. Soc. B.* 2812014088220140882. <http://doi.org/10.1098/rspb.2014.0882>, 2014.
- Bradley, JA; Anesio, AM; Arndt, S.: Microbial and biogeochemical dynamics in glacier forefields are sensitive
to century-scale climate and anthropogenic change, *Frontiers in Earth Science*, v.5, p.26, 2017.
- 595 Brooks, P.D., Schmidt, S.K. and Williams, M.W.: Winter production of CO₂ and N₂O from alpine tundra:
environmental controls and relationship to inter-system C and N fluxes. *Oecologia*, 110(3), pp.403-413, 1997.
- 600 Cimpoiașu, M. O., Kuras, O., Pridmore, T., & Mooney, S. J.: Potential of geoelectrical methods to monitor root
zone processes and structure: A review. *Geoderma*, 365. <https://doi.org/10.1016/j.geoderma.2020.114232>, 2020.
- Cimpoiașu, M. O., Kuras, O., Wilkinson, P. B., Pridmore, T., & Mooney, S. J.: Hydrodynamic characterization
of soil compaction using integrated electrical resistivity and X-ray computed tomography. *Vadose Zone Journal*,
20(4), 1–15, <https://doi.org/10.1002/vzj2.20109>, 2021.
- 605 Cimpoiașu, M. O., Kuras, O., Harrison, H., Wilkinson, P., Meldrum, P., Chambers, J., Oroza, C., Liljestrand, D.,
Irons, T., Schmidt, S., Sommers, P. and Bradley, J.: Characterisation of a deglaciated sediment chronosequence in
the High Arctic Using Near-Surface Geophysical Monitoring, *Permafrost and Periglacial processes*, Accepted for
publication, 2024.
- 610 Commane, R., Lindaas, J., Benmergui, J., Luus, K.A., Chang, R.Y.W., Daube, B.C., Euskirchen, E.S., Henderson,
J.M., Karion, A., Miller, J.B. and Miller, S.M.: Carbon dioxide sources from Alaska driven by increasing early
winter respiration from Arctic tundra. *Proceedings of the National Academy of Sciences*, 114(21), pp.5361-5366,
2017.
- 615 Dahlin, T., & Zhou, B.: Multiple-gradient array measurements for multichannel 2D resistivity imaging. *Near
Surface Geophysics*, 4(2), 113–123. <https://doi.org/10.3997/1873-0604.2005037>, 2006.
- 620 Delforge, D., Watlet, A., Kaufmann, O., van Camp, M., & Vanclooster, M.: Time-series clustering approaches
for subsurface zonation and hydrofacies detection using a real time-lapse electrical resistivity dataset. *Journal of
Applied Geophysics*, 184. <https://doi.org/10.1016/j.jappgeo.2020.104203>, 2021.
- 625 Doetsch, J., Ingeman-Nielsen, T., Christiansen, A. v., Fiandaca, G., Auken, E., & Elberling, B.: Direct current
(DC) resistivity and induced polarization (IP) monitoring of active layer dynamics at high temporal resolution.
Cold Regions Science and Technology, 119, 16–28. <https://doi.org/10.1016/j.coldregions.2015.07.002>, 2015.
- 630 Farzamian, M., Vieira, G., Monteiro Santos, F. A., Yaghoobi Tabar, B., Hauck, C., Catarina Paz, M., ... Angel
De Pablo, M. : Detailed detection of active layer freeze-thaw dynamics using quasi-continuous electrical
resistivity tomography (Deception Island, Antarctica), *Cryosphere*, 14(3), 1105–1120. <https://doi.org/10.5194/tc-14-1105-2020>, 2020.
- Freeman, K.R., Pescador, M.Y., Reed, S.C. *et al.*: Soil CO₂ flux and photoautotrophic community composition
in high-elevation, “barren” soils. *Environmental Microbiology*, 11, 674– 686, 2009.
- 635 Elberling, B. and Brandt, K.K.: Uncoupling of microbial CO₂ production and release in frozen soil and its
implications for field studies of arctic C cycling. *Soil Biology and Biochemistry*, 35(2), pp.263-272, 2003.
- Freeman, K.R., Pescador, M.Y., Reed, S.C. *et al.*: Soil CO₂ flux and photoautotrophic community composition
in high-elevation, “barren” soils. *Environmental Microbiology*, 11, 674– 686, 2009.
- 640 Garré, S., Coteur, I., Wongleecharoen, C., Hussain, K., Omsunrarn, W., Kongkaew, T., Hilger, T., Diels, J., &
Vanderborght, J.: Can We Use Electrical Resistivity Tomography to Measure Root Zone Dynamics in Fields with
Multiple Crops? *Procedia Environmental Sciences*, 19(0), 403–410.
<https://doi.org/10.1016/j.proenv.2013.06.046>, 2013.
- 645



- Giuseppe, M.G.D., Troiano, A., Troise, C., Natale, G.D.: K-Means clustering as tool formultivariate geophysical data analysis. An application to shallow fault zone imaging. *J. Appl. Geophys.* 101, 108–115. <https://doi.org/10.1016/j.jappgeo.2013.12.004>, 2014.
- 650 Giuseppe, M.G.D., Troiano, A., Patella, D., Piochi, M., Carlino, S.: A geophysical k-means cluster analysis of the Solfatara-Pisciarelli volcano-geothermal system Campi Flegrei (Naples, Italy). *J. Appl. Geophys.* 156, 44–54. <https://doi.org/10.1016/j.jappgeo.2017.06.001>, 2018.
- 655 Hamberg, A.: En resa till norra Ishafvet sommaren 1892, *Ymer*, 14, 25–61, 1894.
- Hambrey, M. J., M. R. Bennett, J. A. Dowdeswell, N. F. Glasser and D. Huddart: Debris entrainment and transfer in polythermal valley glaciers, *J. Glaciol.*, 45(149), 69–86, 1999.
- 660 Hauck, C.: Frozen ground monitoring using DC resistivity tomography, *Geophysical Research Letters*, v.29(21), p.12–1–12–4, 2002.
- Hilbich, C., Fuss, C., & Hauck, C.: Automated time-lapse ERT for improved process analysis and monitoring of frozen ground. *Permafrost and Periglacial Processes*, 22(4), 306–319. <https://doi.org/10.1002/ppp.732>, 2011.
- 665 Hodkinson, I. D., Coulson, S. J., & Webb, N. R.: Community assembly along proglacial chronosequences in the high Arctic: Vegetation and soil development in north-west Svalbard, *Journal of Ecology*, 91(4), 651–663, <https://doi.org/10.1046/j.1365-2745.2003.00786.x>, 2003.
- 670 Holmes, J., Chambers, J., Wilkinson, P., Meldrum, P., Cimpoiaşu, M., Boyd, J., ... Donohue, S.: Application of petrophysical relationships to electrical resistivity models for assessing the stability of a landslide in British Columbia, Canada, *Engineering Geology*, 301 (July 2021). <https://doi.org/10.1016/j.enggeo.2022.106613>, 2022.
- 675 Hugelius, G., Strauss, J., Zubrzycki, S., Harden, J.W., Schuur, E.A.G., Ping, C.L., Schirrmeister, L., Grosse, G., Michaelson, G.J., Koven, C.D. and O'Donnell, J.A.: Estimated stocks of circumpolar permafrost carbon with quantified uncertainty ranges and identified data gaps. *Biogeosciences*, 11(23), pp.6573–6593, 2014.
- Irvine-Fynn, T.D.L., Moorman, B.J., Sjogren, D.B., Walter, F.S.A., Willis, I.C., Hodson, A.J., Williams, J.L.M., Mumford, P.N.: Cryological processes implied in Arctic proglacial stream sediment dynamics using principal components analysis and regression. In: Harris, C., Murton, J. (Eds.), *Cryospheric Systems: Glaciers and Permafrost*, Geological Society Special Publication, London, pp. 83–98, 2005.
- 680 Kasprzak, M.: High-resolution electrical resistivity tomography applied to patterned ground, Wedel Jarlsberg Land, south-west Spitsbergen, *Polar Research*, v.34(1), p.25678, 2015.
- 685 Laloy, E., Javaux, M., Vanclooster, M., Roisin, C., & Bielders, C. L.: Electrical Resistivity in a Loamy Soil: Identification of the Appropriate Pedo-Electrical Model. *Vadose Zone Journal*, 10(3), 1023–1033. <https://doi.org/10.2136/vzj2010.0095>, 2011.
- 690 Loke, MH, Chambers, JE; Rucker, DF; Kuras, O; Wilkinson, PB: Recent developments in the direct-current geoelectrical imaging method, *Journal of Applied Geophysics*, v.95, p.135–156, 2013.
- Loke, MH: RES3DINVx64 ver. 4.07 with multi-core and 64-bit support for Windows XP/Vista/7/8/10. Rapid 3-D Resistivity & IP inversion using the least-squares method. *Geoelectrical Imaging 2-D and 3-D*. Geotomo Software, 2017.
- 695 Martín-Moreno, R., Allende Álvarez, F., Hagen, J.O.: Little Ice Age' glacier extent and subsequent retreat in Svalbard archipelago. *The Holocene* 27 (9):1–12. <https://doi.org/10.1177/0959683617693904>, 2017.
- 700 Michot, D., Dorigny, A., & Benderitter, Y.: Mise en évidence par résistivité électrique des écoulements préférentiels et de l'asèchement par le mais d'un CALCISOL de Bauce irrigué. *Sciences de La Terre et Des Planètes*, 332, 29–36, 2001.



- 705 Natali, S.M., Watts, J.D., Rogers, B.M., Potter, S., Ludwig, S.M., Selbmann, A.K., Sullivan, P.F., Abbott, B.W.,
Arndt, K.A., Birch, L. and Björkman, M.P.: Large loss of CO₂ in winter observed across the northern permafrost
region. *Nature Climate Change*, 9(11), pp.852-857, 2019.
- 710 Nielsen, C.B., Groffman, P.M., Hamburg, S.P., Driscoll, C.T., Fahey, T.J. and Hardy, J.P.: Freezing effects on
carbon and nitrogen cycling in northern hardwood forest soils. *Soil Science Society of America Journal*, 65(6),
pp.1723-1730, 2001.
- NPI:Geologi,Svalbard,https://geodata.npolar.no/arcgis/rest/services/Basisdata/NP_Basiskart_Svalbard_WMTS_25833/MapServer/WMTS/1.0.0/WMTSCapabilities.xml, last accessed 16th November 2023.
- 715 Rapaić, M., Brown, R., Markovic, M. and Chaumont, D.: An evaluation of temperature and precipitation surface-
based and reanalysis datasets for the Canadian Arctic, 1950–2010. *Atmosphere-Ocean*, 53(3), pp.283-303, 2015.
- 720 Rawlins, M.A., Steele, M., Holland, M.M., Adam, J.C., Cherry, J.E., Francis, J.A., Groisman, P.Y., Hinzman,
L.D., Huntington, T.G., Kane, D.L. and Kimball, J.S.: Analysis of the Arctic system for freshwater cycle
intensification: Observations and expectations. *Journal of Climate*, 23(21), pp.5715-5737, 2010.
- 725 Raz-Yaseef, N., Torn, M.S., Wu, Y., Billesbach, D.P., Liljedahl, A.K., Kneafsey, T.J., Romanovsky, V.E., Cook,
D.R. and Wulschleger, S.D.: Large CO₂ and CH₄ emissions from polygonal tundra during spring thaw in northern
Alaska. *Geophysical Research Letters*, 44(1), pp.504-513, 2017.
- 730 Rime, T., Hartmann, M., Brunner, I., Widmer, F., Zeyer, J. and Frey, B.: Vertical distribution of the soil microbiota
along a successional gradient in a glacier forefield *Molecular Ecology*, 24: 1091-1108, 2015.
- Samouëlian, A., Cousin, I., Richard, G., Tabbagh, A., & Bruand, A.: Electrical resistivity imaging for detecting
soil cracking at the centimetric scale, *Soil Science Society of America Journal*, 67(5), 1319–1326.
<https://doi.org/10.2136/sssaj2003.1319>, 2003.
- 735 Schmidt, S.K., S.C. Reed, D.R. Nemergut, C.C Cleveland, E.K. Costello, M.N. Weintraub, A.F. Meyer, A.P.
Martin & J.C. Neff.: The earliest stages of ecosystem succession in high-elevation, recently de-glaciated soils,
Proc. Royal Society B, 275: 2793-2802, 2008.
- 740 Seklima: Observations and weather statistics. [online] Available at: <<https://seklima.met.no/>> [Accessed 10th June
2023].
- 745 Teepe, R. and Ludwig, B.: Variability of CO₂ and N₂O emissions during freeze-thaw cycles: results of model
experiments on undisturbed forest-soil cores. *Journal of Plant Nutrition and Soil Science*, 167(2), pp.153-159,
2004.
- 750 Uhlemann, S., Dafflon, B., Peterson, J., Ulrich, C., Shirley, I., Michail, S., & Hubbard, S. S.: Geophysical
Monitoring Shows that Spatial Heterogeneity in Thermohydrological Dynamics Reshapes a Transitional
Permafrost System, *Geophysical Research Letters*, 48(6), 1–11. <https://doi.org/10.1029/2020GL091149>, 2021.
- 755 Wilkinson, P. B., Chambers, J. E., Meldrum, P. I., Kuras, O., Inauen, C. M., Swift, R. T., Curioni, G.,
Uhlemann, S., Graham, J., & Atherton, N.: Windowed 4D inversion for near real-time geoelectrical monitoring
applications. *Frontiers in Earth Science*, 10. <https://doi.org/10.3389/feart.2022.983603>, 2022.
- 760 Wu, Y., Hubbard, S. S., Ulrich, C., & Wulschleger, S. D.: Remote Monitoring of Freeze-Thaw Transitions in
Arctic Soils Using the Complex Resistivity Method. *Vadose Zone Journal*, 12(1), vzj2012.0062.
<https://doi.org/10.2136/vzj2012.0062>, 2013.
- 765 Wu, Y., Nakagawa, S., Kneafsey, T. J., Dafflon, B., & Hubbard, S.: Electrical and seismic response of saline
permafrost soil during freeze - Thaw transition. *Journal of Applied Geophysics*, 146, 16–26.
<https://doi.org/10.1016/j.jappgeo.2017.08.008>, 2017.
- 770 Yi, Y., Kimball, J. S., Rawlins, M. A., Moghaddam, M., and Euskirchen, E. S.: The role of snow cover affecting
boreal-arctic soil freeze–thaw and carbon dynamics, *Biogeosciences*, 12, 5811–5829, <https://doi.org/10.5194/bg-12-5811-2015>, 2015.



- 765 Zhang, T.: Influence of the seasonal snow cover on the ground thermal regime: An overview. *Reviews of Geophysics*, 43(4), 2005.
- Zona, D., Gioli, B., Commane, R., Lindaas, J., Wofsy, S.C., Miller, C.E., Dinardo, S.J., Dengel, S., Sweeney, C., Karion, A. and Chang, R.Y.W.: Cold season emissions dominate the Arctic tundra methane budget. *Proceedings of the National Academy of Sciences*, 113(1), pp.40-45, 2016.